Observing Nitrogen Dioxide Air Pollution Inequality Using High-Spatial-Resolution Remote Sensing Measurements in Houston, Texas

Mary Angelique G. Demetillo, Aracely Navarro, Katherine K. Knowles, Kimberly P. Fields, Jeffrey A. Geddes, Caroline R. Nowlan, Scott J. Janz, Laura M. Judd, Jassim Al-Saadi, Kang Sun, Brian C. McDonald, Glenn S. Diskin, and Sally E. Pusede*

Cite This: https://dx.doi.org/10.1021/acs.est.0c01864

Read Online

ACCESS | Metrics & More | Article Recommendations | Supporting Information

ABSTRACT: Houston, Texas is a major U.S. urban and industrial area where poor air quality is unevenly distributed and a disproportionate share is located in low-income, non-white, and Hispanic neighborhoods. We have traditionally lacked city-wide observations to fully describe these spatial heterogeneities in Houston and in cities globally, especially for reactive gases like nitrogen dioxide (NO_2). Here, we analyze novel high-spatial-resolution (250 m × 500 m) NO_2 vertical columns measured by the NASA GCAS airborne spectrometer as part of the September-2013 NASA DISCOVER-AQ mission and discuss differences in population-weighted NO_2 at the census-tract level. Based on the average of 35 repeated flight circuits, we find 37 ± 6% higher NO_2 for non-whites and Hispanics living in low-income tracts (LIN) compared to whites living in high-income tracts (HIW) and report NO_2 disparities separately by race ethnicity (11−32%) and poverty status (15−28%). We observe substantial time-of-day and day-to-day variability in LIN-HIW NO_2 differences (and in other metrics) driven by the greater prevalence of NO_x ($\equiv NO + NO_2$) emission sources in low-income, non-white, and Hispanic neighborhoods. We evaluate measurements from the recently launched satellite sensor TROPOMI (3.5 km × 7 km at nadir), averaged to 0.01° × 0.01° using physics-based oversampling, and demonstrate that TROPOMI resolves similar relative, but not absolute, tract-level differences compared to GCAS. We utilize the high-resolution FIVE and NEI NO_x inventories, plus one year of TROPOMI weekday−weekend variability, to attribute tract-level NO_2 disparities to industrial sources and heavy-duty diesel trucking. We show that GCAS and TROPOMI spatial patterns correspond to the surface patterns measured using aircraft profiling and surface monitors. We discuss opportunities for satellite remote sensing to inform decision making in cities generally.
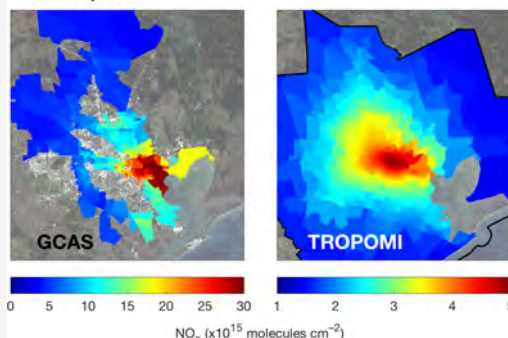
INTRODUCTION

Houston, Texas is a large, socio-demographically diverse U.S. city that is also a global center for petrochemical manufacturing. Houston experiences among the worst air quality in the United States[1,2] with documented evidence that local air pollution disproportionately burdens the city's low-income residents and communities of color,[3−5] leading to demonstrated differences in health and life expectancy as a result.[6,7] Similar racial, ethnicity, and income-based inequalities have also been observed in other major U.S. cities.[8−13] Our ability to describe intra-urban pollutant variability has been limited by the lack of spatially continuous, temporally resolved measurements that capture gradients between neighborhoods. In the case of reactive gases with short atmospheric lifetimes, such as nitrogen dioxide (NO_2), intra-urban spatiotemporal variability cannot be directly observed by traditional monitoring approaches, impeding efforts to address air quality disparities through policy.

NO_2 plays a critical role in surface air quality, and knowledge of NO_2 spatiotemporal variability is fundamental to air pollution and public health decision making. NO_2 is a key control over the atmospheric oxidation capacity, a precursor to ground-level ozone and particulate matter (PM), and a regulated criteria pollutant under the Clean Air Act. In U.S. cities, NO_2 emissions are typically dominated by mobile sources and fossil-fuel-based electricity generation;[14] in Houston, petrochemical refineries and industrial activities are also large emitters.[15−17] NO_2 is a robust indicator of combustion emissions generally[10] and a common surrogate

for traffic-pollutant mixtures, especially toxic diesel exhaust.[18] Epidemiological studies have linked ambient NO_2 concentrations to adverse health outcomes,[19−22] and residential proximity to roadways (determined using geospatial and/or NO_2 datasets) has been associated with reduced lung function and asthma,[23−25] cardiac and pulmonary mortality, and preeclampsia and preterm birth.[26−28]

NO_2 concentrations change rapidly in the near-field of sources with downwind distance-decay gradients, largely controlled by rates of dispersion, ranging from <0.5 km in unstable to 1−2 km in stable atmospheres.[29,30] Widely used monitoring tools such as regulatory surface networks and satellite instruments have historically been unable to resolve such NO_2 gradients. Across the United States, there are over 400 in situ NO_2 monitoring stations (typically measuring NO_2*, representing NO_2 plus a positive measurement bias), yet fewer than 1/3 of U.S. urban areas are equipped with even one analyzer.[31] In cities with monitors, monitoring stations are spatially sparse, and, while urban NO_2 is well correlated with traffic, U.S. Environmental Protection Agency (EPA) guidance generally recommends siting monitors away from roadways.[31,32] At the same time, satellite remote sensing has contributed substantially to our understanding of inter-urban NO_2 distributions,[31,33−35] providing spatially continuous maps of NO_2 columns across cities, but mostly lacked the resolution required to capture intra-urban variability. The Ozone Monitoring Instrument (OMI) with a nadir footprint of 13 km × 24 km has previously been shown to detect near-surface NO_2 variability within large cities,[31,36] including individual slant-column observations when operated in the "super-zoom" mode (13 km × 3 km).[37] Fine spatial scale land-use regression (LUR) models, which predict NO_2 concentrations as a function of the geographic location of emitters and other land cover elements, have added spatial detail to coarse NO_2 datasets[38−40] and allowed the creation of NO_2 maps at resolutions of 100 m × 100 m, fine enough to resolve distance-decay gradients away from sources. However, these models require substantial a priori geospatial knowledge that may not be available and rely on temporal averages of pollutant data of at least weeks (surface monitors) to months (satellites). As a result, LUR models typically do not describe NO_2 temporal variability, hindering source identification and discovery using time-varying emission patterns and leading to biases in acute exposure epidemiological studies related to confounding temporal trends and meteorology[18] with analyses based on emission inventories and pollutant proxies, e.g., neighborhood distance to roadways, facing similar limitations.

Here, we evaluate the extent that higher-resolution NO_2 remote sensing can resolve intra-urban spatiotemporal variability relevant to NO_2 inequality in Houston, Texas. First, we describe an observationally based analysis using novel fine-spatial-resolution (250 m × 500 m), sub-orbital remote sensing measurements from NASA GCAS (GEOstationary Coastal and Air Pollution Events (GEO-CAPE) Airborne Simulator)[41−43] collected as part of the September 2013 DISCOVER-AQ study (Deriving Information on Surface Conditions from COlumn and VERtically Resolved Observations Relevant to Air Quality). We quantify neighborhood-level (census-tract) differences in population-weighted tropospheric NO_2 vertical columns, with GCAS columns resolving census-tract variability, and discuss atmospheric controls over the NO_2 spatiotemporal distribution for various socio-demographic groups, specifically race-ethnicity and income. Second, we

test whether the recently launched satellite-based TROPOMI sensor, currently producing the highest spatial resolution NO_2 satellite measurements over North America, precisely and/or accurately captures the same NO_2 column differences detected by GCAS. We utilize in situ NO_2 vertical profiles collected onboard the NASA P-3B during DISCOVER-AQ and data from the routine surface monitoring network to demonstrate that columns and surface measurements represent similar NO_2 spatial patterns. We evaluate major source contributions to census-tract-level NO_2 disparities, comparing weekday—weekend column differences in the first full year of TROPOMI data (June 2018 to May 2019) to estimates derived from emissions in the high-resolution Fuel-based Inventory of Vehicle Emissions (FIVE) and National Emission Inventory (NEI). Finally, we discuss potential applications and limitations of next-generation satellite observations to inform, evaluate, enforce, and motivate decision making on air pollution inequality in U.S. cities.

■ MATERIALS AND METHODS

Houston, Texas. Houston—The Woodlands—Sugar Land, referred to in this paper as either Houston or the Houston Metropolitan Area (HMA), is the largest metropolitan statistical area in Texas and among the largest in the U.S. with 6.1 million residents in 2013 and 6.8 million in 2018.[44] Houston is a growing city that is racially, ethnically, and economically diverse and home to one of the largest Hispanic populations in the U.S. Houston is also the location of ~1/4 of all U.S. chemical refineries[45] and the Houston Ship Channel (HSC), a busy waterway where numerous major industrial facilities are located, extending from the Gulf of Mexico, through Galveston Bay, and along the Buffalo Bayou river between Baytown and Downtown Houston (Figure S1).[46] The unique combination of urban transportation, petrochemical emissions, and the prevalent land—sea breeze[47] contribute to the HMA's poor air quality, including high levels of ozone[48] and hazardous air pollutants.[49] Past research has shown that local air pollution is not uniformly distributed across Houston but instead concentrated in neighborhoods with larger Hispanic populations, lower rates of educational attainment, and higher rates of poverty.[3,4] Primarily non-white, Hispanic, and lower-income neighborhoods have experienced greater cancer risks, increased chronic and acute air pollutant exposure, and lower overall physical well-being, especially in communities adjacent to facilities on the HSC where low-income households and people of color are statistically overrepresented.[6,7]

GCAS. The Geostationary Coastal and Air Pollution Events (GEO-CAPE) airborne simulator (GCAS) was developed as a technology demonstration instrument in support of the Geostationary Coastal and Air Pollution Events (GEO-CAPE) decadal survey mission.[50] GCAS makes hyperspectral nadir-viewing measurements of backscattered solar radiation in two channels at wavelengths of 300−490 nm (air quality species) and 480−900 nm (ocean color). Each channel uses a two-dimensional charge-coupled device (CCD) array detector for mapping with one CCD dimension capturing absorption spectra and the other providing cross-track spatial coverage over an ~45° field of view. GCAS NO_2 column retrievals consisted of a two-step approach similar to algorithms used for other major satellite instruments: GOME, SCIAMACHY, OMI, TROPOMI, and the forthcoming TEMPO.[41,42] First, NO_2 slant column densities were derived by direct spectral

fitting of radiances using measured nadir spectra and an averaged unpolluted reference spectrum (over the Gulf of Mexico). Second, slant columns were converted to vertical columns using an air mass factor (AMF), which was a function of the observing geometry, surface reflectance, ozone profile, and trace gas profile shape. AMFs were calculated for each scene with scattering weights derived from a radiative transfer model over 56 vertical layers, 45 of which were generated from the Community Multi-scale Air Quality (CMAQ). CMAQ (version 5.0.2) was run at a spatial resolution of 4 km × 4 km, temporal resolution of 20 min, and vertical resolution ranging from 22 m (surface) to ∼200 m (2 km) to ∼650 m (aircraft altitude) with offline meteorology driven by the Advanced Research Weather and Forecasting (WRF-ARW) model[51] using the Meteorology-Chemistry Interface Processor (MCIP).[52] Details on the CMAQ and WRF modeling can be found in the work of Loughner and Follette-Cook,[53] and further details on other aspects of the GCAS instrument and retrieval can be found in the work of Nowlan et al.[41,42] GCAS column uncertainties were estimated to range between 20 and 50% and 18 and 30% over moderately ($0.5-1 \times 10^{16}$ molecules cm^{-2}) and heavily polluted ($>2 \times 10^{16}$ molecules cm^{-2}) areas, respectively.[41] Column uncertainties were driven by uncertainties in the AMF and challenges associated with representing species exhibiting high spatiotemporal variability as means. Nowlan et al.[41] reported a small bias (+2%) in the GCAS columns from the use of CMAQ-modeled NO_2 profiles. GCAS observed individual spectra with native spatial resolution on the order of tens of square meters, but spectra were spatially averaged to enhance their signal-to-noise ratio. At a 9 km flight altitude, GCAS produced NO_2 vertical columns at 250 m (across track) × 500 m (along track) with the along-track coverage generated by the host aircraft.

During the Houston DISCOVER-AQ deployment, GCAS flew onboard the NASA B-200 and conducted a total of 21 air quality flights in the morning (8 am−12 pm, LT) and afternoon (1 pm to 5 pm, LT) over 11 days. In this analysis, we focused on measurements of cloud-free pixels from nine weekdays that included both morning and afternoon research flights, typically with two circuits during each flight: September 4, 6, 11−13, 18, and 24−26, 2013. Data from the second circuit of the morning flight of September 12 were omitted because of heavy clouds.

TROPOMI. The TROPOspheric Monitoring Instrument (TROPOMI) is one of the newest space-based NO_2 sensors[54,55] and the single payload onboard the sun-synchronous Copernicus Sentinel-5 Precursor (S5P) satellite. TROPOMI measures in the ultraviolet and visible (270−500 nm), near-infrared (675−775 nm), and shortwave infrared (2305−2385 nm) spectral regions to quantify a range of atmospheric trace gases. NO_2 is retrieved by fitting the 405−465 nm band using an updated OMI DOMINO algorithm and based on work from the QA4ECV project.[56−60] At nadir, NO_2 is retrieved at a spatial resolution of 3.5 km × 7 km for the time period of this study.[54,55] Precision of individual tropospheric NO_2 columns over urban/polluted scenes is on the order of 30−60%[61] and dominated by uncertainties in the AMF. Key inputs to the AMF are: clouds; the NO_2 profile shape, generated using 1° × 1° TM5-MP model output;[62] and the surface albedo, from a 0.5° × 0.5° monthly OMI climatology.[63] We used Level 2 NO_2 tropospheric columns, quality descriptor: qa value of >0.75 as recommended by the Product User Manual.[64]

TROPOMI maps at 0.01° × 0.01° were produced using physics-based oversampling. In brief, the approach represents observations on the ground as sensitivity distributions, rather than as points or polygons. For image grating spectrometers like TROPOMI, generalized two-dimensional super Gaussian functions have been shown to best characterize the sensitivity distributions. For details on the oversampling method, see Sun et al.[65]

Surface NO_2^* and Winds. Hourly ground-based nitrogen dioxide (NO_2^*), wind speed, and wind direction measurements were downloaded via the Texas Commission on Environmental Quality Data Report query tool (https://www17.tceq.texas.gov/tamis/index.cfm). NO_2^* was measured using chemiluminescence coupled to a heated molybdenum converter that includes a positive interference from nitric acid and organic nitrates,[66] which largely affects absolute rather than relative NO_2^* mixing ratios.[67] We use the nomenclature NO_2^* rather than NO_2 in acknowledgment of this interference. For September 2013, we analyzed wind data from 16 monitoring stations in the HMA with simultaneous NO_2^* and wind observations. To observe interannual trends, we compared daytime (10 am to 4 pm LT) annual averaged data for June 2013 to May 2014 and June 2018 to May 2019 using NO_2^* measurements from the 15 stations operating in both time periods. To compare surface and TROPOMI column observations, we included mean midday (12−3 pm LT) measurements from all 17 monitors in the HMA, excluding two designated near-roadway sites[68] (see Figure S14 caption for station information).

Demographic Data and Boundaries. Household income statistics from the 2010 American Community Survey: five-year dataset and race-ethnicity population tables from the 2010 U.S. Census were downloaded from the IPUMS National Historical Geographic Information System.[69] Year 2013 census tract polygons were downloaded as TIGER/Line shape files from the data.gov library: https://www.census.gov/cgi-bin/geo/shapefiles/index.php.

P-3B Dataset and Convective Boundary Layer (CBL) Height Determination. As part of DISCOVER-AQ, NO_2 and NO were measured onboard the NASA P-3B at a 1 s time resolution by the NCAR chemiluminescence system, detecting NO directly and NO_2 following photolysis into NO by a blue light converter. The instrument was calibrated frequently in flight, and uncertainties were 0.02 ppb in precision (at 1 s averaging) and ±10% accuracy for NO_2. $H_2O_{(v)}$ was measured by the NASA open-path diode laser hygrometer (DLH) and reported at 1 s time resolution with overall uncertainties of 5%. Static air temperature data were collected by a Rosemount model 102 sensor with a precision of 0.006 °C and accuracy of ±0.2 °C.

For each P-3B profile, we identified the CBL height as the altitude of the strongest coincident gradients in potential temperature (θ) and water vapor mixing ratio ($H_2O_{(v)}$),[70] which were also near the top of the region of constant $H_2O_{(v)}$ mixing ratios extending from the surface.[71] To reduce spurious layer determination from instrument noise, we first averaged measurements into 10 m altitude bins and calculated 5-point running mean lapse rates and $H_2O_{(v)}$ gradients. Individual CBL heights for each profile are given in Table S2. Vertical profiles of NO_2, lapse rate, θ, and $H_2O_{(v)}$ with their corresponding CBL heights over Moody Tower, Channelview, Deer Park, West Houston, Conroe, and Manvel Croix are provided in the Supporting Information.
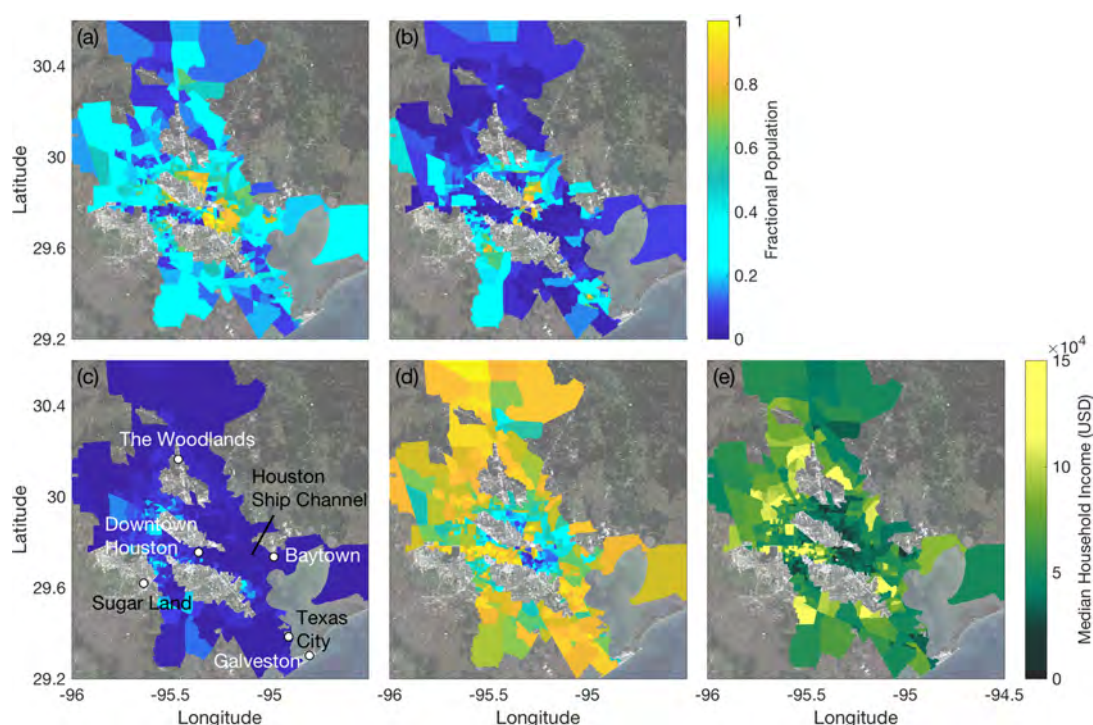
Figure 1. Fractional census-tract-level race-ethnicity demographics along the GCAS flight tract: (a) Hispanics, (b) Black and African Americans, (c) Asians, and (d) non-Hispanic whites. Panel (c) includes labels for various locations within the HMA. (e) Fractional median annual household income in USD. While the aircraft flew a repeated circuit, there were slight variations in some circuits between flights; this exact circuit is from the morning of September 4. Background map data: Landsat 8 composite over January 2017 to June 2018.

FIVE and NEI Inventories. The Fuel-based Inventory of Vehicle Emissions (FIVE) is a spatially (500 m × 500 m) and temporally (monthly) resolved inventory of mobile source emissions (on-road + off-road engines).[72] FIVE provided on-road emissions derived from publicly available fuel sales reports, road-level traffic counts, and time-resolved weigh-in-motion traffic counts.[73] Fuel use uncertainties are based on differences between fuel sale reports and truck travel (±13% in Texas) and traffic count site selection and sample size (±10% for major roads and freeways in large urban areas). Emissions uncertainties were derived from regression analysis of near-road infrared remote sensing and tunnel studies: ±16% and ±15% for light-duty gasoline vehicles and heavy-duty diesel trucks, respectively.[72] We focused on annual averages of the on-road component, which was comprised of light-duty gasoline vehicles and heavy-duty trucks with fuels sales and emission factors updated to 2018.

The National Emissions Inventory (NEI) provides a comprehensive and detailed estimate of NO_2 emissions from stationary sources, including industrial facilities, power plants, airports, and commercial facilities. We used estimates from the 2014 NEI Version 1, encompassing reports from state, local, and tribal air agencies and the EPA programs: Toxic Release Inventory, Acid Rain Program, and Maximum Achievable Control Technology standards development. Emission uncertainties in power plants were ±25%,[74] and errors in industrial facilities and other less-characterized stationary sources were assumed to be ±50%.[75]

Population-Weighted NO_2 and Census-Tract-Level NO_2 Differences. GCAS and TROPOMI NO_2 columns were averaged within census tract polygons and tagged with geographic identifiers. Population-weighted NO_2 columns were calculated as equal to the product of the tract-unit NO_2 column ($NO_{2,j}$) and demographic group population (p_j) (by race ethnicity or poverty classification) in the ith tract, summed over all census tracts with NO_2 data (n) and divided by the summation of the group population (p_j) (eq 1). Errors were defined as standard mean errors with N representing the number of census tracts with both NO_2 observations and residents of a given demographic group.

$$\text{population-weighted } NO_{2,j} = \sum_{i=1}^{n} NO_{2,i}\, p_{i,j} \Big/ \sum_{i=1}^{n} p_{i,j} \tag{1}$$

We discussed absolute and relative NO_2 inequality in terms of the absolute and percent difference in population-weighted NO_2 columns between two demographic groups. Race-ethnicity demographics were defined with the following U.S. Census codes: Black and African Americans (JMJE004), excluding individuals identifying as Hispanic or Latino; Asians (JMJE006), excluding those identifying as Hispanic or Latino; Hispanics (JMJE012), including all races reporting as Hispanic; and non-Hispanic whites (JMJE003). GCAS sampling was statistically representative of race-ethnicity demographics in the HMA (GCAS, HMA): Black and African American (17%, 12%), Asian (5%, 4%), Hispanic (36%, 37%), and non-Hispanic white (42%, 47%). Census-tract-level race, ethnicity, and income variability along the GCAS flight track is shown in Figure 1. We calculated NO_2 for non-whites and Hispanics living in low-income tracts, denoted as LIN, by first applying an income threshold of census-tract median household incomes of <35,000 USD and then computing population-weighted NO_2 columns in the low-income tracts for Black and African Americans, Asians, and Hispanics. Likewise, we calculated NO_2 columns for whites living in high-income tracts (HIW), applying the income threshold of
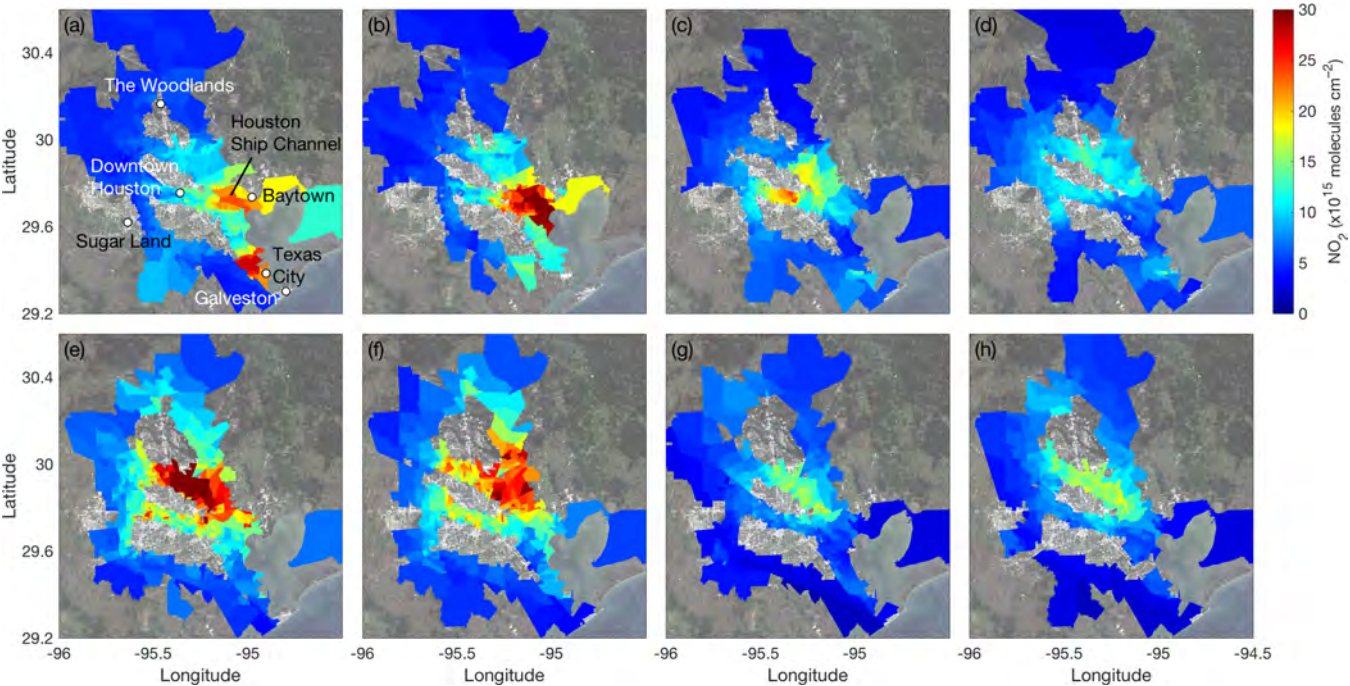
Figure 2. GCAS NO_2 column densities (molecules cm^{-2}) averaged to census tracts on two sample days, (a−d) September 4 (top row) and (e−h) 26 (bottom row), during eight flight circuits in the early morning (8 am−10 am LT; panels a and e), late morning (10 am−12 pm LT; panels b and f), early afternoon (1 pm−3 pm LT; panels c and g), and late afternoon (3 pm−5 pm LT; panels d and h). Background map data: Landsat 8 composite, January 2017−June 2018.

Table 1. Census-Tract-Averaged Population-Weighted NO_2 Columns (molecules cm^{-2}) for Weekdays (Tuesday−Friday) during Morning and Afternoon GCAS Flights (Average of the Two Circuits) with Variability Reported as Two Standard Deviations of Individual Circuit Population-Weighted NO_2 Means for Different Socio-Demographic Categories; Annual (June 2018 to May 2019) TROPOMI Observations Sub-sampled along the GCAS Flight Track (September 4, Morning) on Weekdays and for the HMA on Weekdays and Weekends (Saturday−Sunday); September 2018 Weekday TROPOMI Observations, both along the GCAS Flight Track (September 4, Morning) and for the Full HMA[a]

	population-weighted census-tract-averaged NO_2 ($\times 10^{15}$ molecules cm^{-2})								
	GCAS weekday flights				TROPOMI				
	means		variability (2σ)		annual (along GCAS)	annual (HMA)		September (along GCAS)	September (HMA)
group	morning	afternoon	morning	afternoon	weekdays	weekdays	weekends	weekdays	weekdays
LIN	13.9 ± 0.5	9.0 ± 0.3	15.3	4.3	3.7 ± 0.1	3.3 ± 0.1	2.6 ± 0.1	4.7 ± 0.1	4.0 ± 0.1
HIW	9.1 ± 0.4	6.3 ± 0.3	4.2	2.4	2.7 ± 0.1	2.2 ± 0.1	1.9 ± 0.1	3.1 ± 0.1	2.9 ± 0.1
below-poverty	13.0 ± 0.4	8.4 ± 0.3	13.7	4.1	3.5 ± 0.1	3.1 ± 0.1	2.1 ± 0.1	4.4 ± 0.1	3.7 ± 0.1
near-poverty	11.3 ± 0.2	7.5 ± 0.1	9.8	3.3	3.2 ± 0.1	2.9 ± 0.1	2.0 ± 0.1	4.0 ± 0.1	3.4 ± 0.1
above-poverty	9.5 ± 0.3	6.5 ± 0.2	5.1	2.5	2.8 ± 0.1	2.6 ± 0.1	1.9 ± 0.1	3.4 ± 0.1	2.9 ± 0.1
Hispanic	12.8 ± 0.4	8.4 ± 0.2	13.3	3.9	3.5 ± 0.1	3.3 ± 0.1	2.2 ± 0.1	4.5 ± 0.1	4.0 ± 0.1
Black/African American	11.4 ± 0.4	7.2 ± 0.2	8.3	3.3	3.2 ± 0.1	3.0 ± 0.1	2.1 ± 0.1	3.9 ± 0.1	3.4 ± 0.1
Asian	10.4 ± 0.3	6.7 ± 0.2	3.3	2.4	3.0 ± 0.1	2.8 ± 0.1	2.0 ± 0.1	3.6 ± 0.1	3.3 ± 0.1
white	8.8 ± 0.3	6.2 ± 0.2	4.9	2.7	2.7 ± 0.1	2.3 ± 0.1	1.7 ± 0.1	3.1 ± 0.1	2.5 ± 0.1

[a]GCAS and TROPOMI uncertainties are standard mean errors rounded up to at least one decimal position.

census-tract median household incomes of >80,000 USD then computing population-weighted NO_2 columns in high-income tracts for non-Hispanic whites. For reference, lower (upper) annual household-income quintiles were 34,588 (84,905) USD along the GCAS flight path and 33,860 (79,332) USD across the nine counties of the HMA. Along the GCAS track, 13% of the population met the criteria for LIN (16% for HIW), residing in 18% of census tracts (23% for HIW); in the HMA, 16% of the population met the criteria for LIN (13% for HIW), residing in 25% percent of tracts (17% for HIW). Poverty status was categorized following the U.S. Census Bureau

definition using the household income-to-poverty ratio. Households were classified as being below the poverty line if their income was less than the poverty threshold in the U.S. Federal Poverty Guidelines, which scales with the number of people per household. We defined census tracts as below poverty if >20% of households in the tract were at or below an income-to-poverty ratio of 1. The corresponding number of households was used in eq 1. Households with an income-to-poverty ratio greater than 1 in the remaining census tracts comprise the above-poverty population. Near-poverty pop-

E

ulations encompassed households in all tracts with an income-to-poverty ratio of 1−1.24.

RESULTS AND DISCUSSION

GCAS, Census-Tract NO_2 Differences, and Temporal Variability. We focused on GCAS measurements from 35 flight circuits, collected on 9 weekdays (Tuesday−Friday) with sampling conducted in both the morning (8 am−12 pm local time, LT) and afternoon (1 pm−5 pm LT) (Figures S2−S10). Observations from two example days are shown in Figure 2 with GCAS vertical columns averaged to the underlying census tracts. To investigate differences in neighborhood-level NO_2, we calculated tract-level race-ethnicity population-weighted mean NO_2 columns for census tracts along the GCAS flight path for each circuit and compared absolute and relative column differences (Tables 1 and 2). Population-weighted NO_2 columns for Hispanic, Black and African American, and Asian residents across all tracts sampled by GCAS were higher than for non-Hispanic whites by 32 ± 11%, 19 ± 7%, and 11 ± 5%, respectively (Table 1). In census tracts defined as below or near the poverty line, NO_2 columns were on average 28 ± 11% and 15 ± 8% higher than those above the poverty line. For non-whites and Hispanics in low-income tracts, population-weighted NO_2 columns were 37 ± 6% higher than for HIWs. Correspondingly, predominantly Hispanic and Black/African American neighborhoods and lower-income neighborhoods of all races and ethnicities were more often located in central Houston and in closer proximity to the HSC (Figure 1). Because we utilized population-weighted columns, our results do not simply reflect urban−rural gradients. In the U.S. Census-designated "urbanized areas" only (Figure 3b), population-weighted NO_2 columns for Hispanic, Black and African American, and Asian residents were 21 ± 5%, 13 ± 6%, and 3 ± 6% higher than for whites, respectively. In census tracts below and near the poverty line, population-weighted NO_2 columns were 24 ± 6% and 14 ± 5% higher than for those above the poverty line, and, for LINs, population-weighted NO_2 columns were 31 ± 8% higher than for HIWs. Nowlan et al.[41] reported that GCAS was found to underestimate NO_2 columns compared to DISCOVER-AQ P-3B measurements for higher column densities with GCAS lower by 10% and overestimate columns near background concentrations with GCAS higher by $\sim 1.6 \times 10^{15}$ molecules cm^{-2}. As a result, census-tract-level NO_2 differences reported here are likely biased low and NO_2 inequalities are underestimated.

While population-weighted NO_2 columns were always higher for LINs than for HIWs, a wider range of NO_2 levels were observed in predominantly non-white, Hispanic, and low-income tracts (Table 2). Variability, defined as two standard deviations of mean population-weighted NO_2 for all 35 flight circuits, was a factor of 2.5 greater for LINs than HIWs. On September 25, meteorological conditions contributed to late-morning NO_2 columns and LIN-HIW differences (84 ± 9%) that were uniquely high (Table 2 and Figure S9); however, even after removing all September 25 data, population-weighted NO_2 columns were still 1.8 times more variable for LINs than HIWs. In the afternoon on all days, absolute NO_2 column densities were lower for both LINs and HIWs than in the morning. Afternoon mean surface winds were 8 ± 1 m s^{-1} and usually from the southeast (onshore flow); by comparison, morning surface winds were 6 ± 2 m s^{-1} and, while typically from the east/east northeast, more varied in direction (Table S1). The observed variability indicated greater NO_x emission

Table 2. GCAS Census-Tract-Averaged Population-Weighted NO_2 Columns (molecules cm^{-2}) for Each Flight Circuit between LINs and HIWs and Their Percent Difference[a]

	morning						afternoon					
	first circuit			second circuit			third circuit			fourth circuit		
	population-weighted NO_2 ($\times 10^{15}$ molecules cm^{-2})		difference (%)	population-weighted NO_2 ($\times 10^{15}$ molecules cm^{-2})		difference (%)	population-weighted NO_2 ($\times 10^{15}$ molecules cm^{-2})		difference (%)	population-weighted NO_2 ($\times 10^{15}$ molecules cm^{-2})		difference (%)
September	LIN	HIW		LIN	HIW		LIN	HIW		LIN	HIW	
4	10.0 ± 0.4	7.5 ± 0.3	28 ± 5	12.4 ± 0.5	8.3 ± 0.5	39 ± 7	12.3 ± 0.5	7.8 ± 0.5	44 ± 7	9.9 ± 0.2	7.4 ± 0.4	28 ± 4
6	11.8 ± 0.4	8.9 ± 0.4	28 ± 6	7.6 ± 0.3	6.0 ± 0.3	24 ± 6	8.6 ± 0.4	6.0 ± 0.3	36 ± 7	7.2 ± 0.4	5.9 ± 0.3	21 ± 5
11	12.4 ± 0.5	8.1 ± 0.4	42 ± 7	10.2 ± 0.5	8.3 ± 0.6	20 ± 9	7.9 ± 0.4	5.7 ± 0.4	33 ± 9	8.0 ± 0.4	6.3 ± 0.4	23 ± 6
12	11.1 ± 0.4	8.7 ± 0.4	25 ± 6				7.7 ± 0.3	4.8 ± 0.2	47 ± 7	10.2 ± 0.5	6.5 ± 0.3	45 ± 6
13	13.7 ± 0.6	9.0 ± 0.5	41 ± 7	11.8 ± 0.5	10.2 ± 0.5	14 ± 7	8.3 ± 0.4	5.3 ± 0.2	45 ± 7	8.6 ± 0.4	5.7 ± 0.2	41 ± 3
18	9.4 ± 0.5	8.0 ± 0.3	17 ± 7	8.7 ± 0.4	7.6 ± 0.4	13 ± 7	6.6 ± 0.2	5.4 ± 0.2	19 ± 5	7.0 ± 0.3	5.7 ± 0.2	20 ± 3
24	8.5 ± 0.3	8.1 ± 0.4	4 ± 6	6.3 ± 0.3	6.2 ± 0.2	2 ± 6	5.7 ± 0.2	4.8 ± 0.2	17 ± 5	6.6 ± 0.2	5.7 ± 0.2	15 ± 3
25	23.9 ± 0.9	13.1 ± 0.7	58 ± 6	37.8 ± 1.9	15.4 ± 1.3	84 ± 9	12.6 ± 0.5	8.9 ± 0.5	35 ± 6	13.8 ± 0.5	10.0 ± 0.5	32 ± 4
26	21.2 ± 1.0	11.2 ± 0.4	61 ± 7	17.3 ± 0.7	12.4 ± 0.5	34 ± 6	10.3 ± 0.4	5.8 ± 0.2	55 ± 6	12.0 ± 0.4	7.0 ± 0.2	44 ± 3
mean	13.0 ± 0.6	9.2 ± 0.4	34 ± 8	14.0 ± 0.6	9.3 ± 0.5	40 ± 8	8.9 ± 0.4	6.0 ± 0.3	39 ± 6	9.1 ± 0.4	6.7 ± 0.3	30 ± 6

[a]For individual circuits, uncertainties are standard mean errors of population-weighted NO_2 across all tracts within the flight path. The second morning pass on September 12 was omitted because most of the circuit was not completed and there were too many clouds.
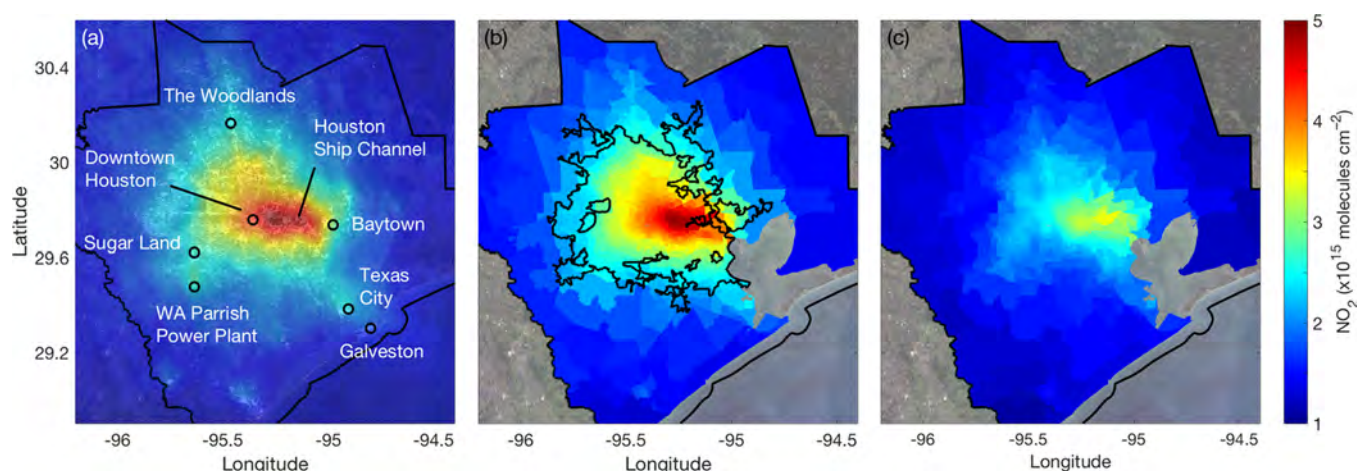
Figure 3. (a) Weekday (Tuesday−Friday) TROPOMI NO$_2$ column densities (molecules cm^{-2}) for June 2018−May 2019 at 0.01° × 0.01° over the greater Houston area and (b) averaged within census tracts. (c) Weekend (Saturday−Sunday) TROPOMI NO$_2$ columns averaged within census tracts for the HMA. A 40% transparency is applied to the TROPOMI data in panel (a) to see the underlying land cover. The inner black outline in panel (b) depicts the census "urbanized area" and the outer black depicts the HMA. Background map data: Landsat 8 composite, January 2017 to June 2018.

source density in proximity to non-whites living in low-income neighborhoods as the highest concentrations should co-locate with sources for reactive gases. We test this conclusion against emission inventory data (below) as high-income tracts were also 60% larger than low-income tracts, leading to greater spatial averaging.

Evaluating TROPOMI Observations. GCAS operates as a satellite analog in NASA airborne missions and its high-spatial-resolution observations now provide data for TROPOMI validation.[76] Launched in October 2017, TROPOMI has been shown to generate detailed NO$_2$ column maps, revealing hotspots undetectable by past space-based sensors due to its order of magnitude-improved spatial resolution.[36,77−79] Here, we use the high-spatial-resolution, but limited duration, GCAS dataset to evaluate TROPOMI-derived annual differences in census tract-scale NO$_2$ columns, both along the GCAS flight track and across the HMA. The comparison provides an evaluation of the suitability of TROPOMI observations to resolve key horizontal NO$_2$ gradients for assessing air pollution disparities.

In Figure 3a,b, TROPOMI observations are weekdays (Tuesday−Friday) over June 2018 to May 2019 with data collection occurring at ~1:30 pm LT. Mondays were excluded as they were considered transition days. TROPOMI measured highly localized NO$_2$ column enhancements over the HSC, Texas City Galveston Bay Refinery (the second largest refinery in the U.S.) and the W.A. Parrish Generating Station (a 3.65 GW dual-fired power plant that includes the largest coal-fired plant in Texas at 2.7 GW). To produce TROPOMI maps at 0.01° × 0.01° (~1 km × 1 km over Houston), we employed a physics-based oversampling of daily images.[65] The annual-average weekday NO$_2$ pattern was spatially similar to GCAS measurements on days with slower surface winds, onshore afternoon air flows, and higher-than-average NO$_2$, in particular, September 4, 25, and 26.

Population-weighted annual weekday TROPOMI columns were 31 ± 3% higher for LINs than for HIWs when sampled along the GCAS flight track (Figure S11). Across the full HMA (Figure 3b and Table 1), weekday TROPOMI observations indicated 34 ± 2% higher population-weighted NO$_2$ columns for LINs than for HIWs. In Houston's "urbanized areas" only

(Figure 3b), which included 79% of tracts in the HMA, population-weighted LIN NO$_2$ columns were 27 ± 3% higher than for HIWs. Finally, in the month of September only (2018), LIN population-weighted weekday TROPOMI NO$_2$ columns were 42 ± 3% greater than for HIWs. Results from both annual and September TROPOMI weekday means agreed with the corresponding GCAS LIN-HIW differences measured during the third circuit (1−3 pm) of 39 ± 6% to within uncertainties. Between 2013 and 2018, surface-level NO$_2$* mixing ratios averaged across the HMA decreased by 6 ± 5% (1.0 ± 7 ppb) with no major changes in the NO$_2$* spatial distribution and lower absolute and relative changes recorded at monitors nearest to the HSC compared to sites in suburban HMA (Figure S12).

In addition to somewhat lower relative LIN-HIW differences, the annually averaged TROPOMI results yielded lower absolute weekday LIN-HIW differences (9.19 × 10^{14} molecules cm^{-2}) compared to those from GCAS (2.6 × 10^{15} molecules cm^{-2}). Temporally averaging TROPOMI observations over the course of a year would have reduced the impact of individual high pollution episodes that exacerbated inequality, such as on September 25, and led to smaller LIN-HIW differences compared to September means; declines in overall NO$_2$ between 2013 and 2018 may have played a role as well. Lower absolute column densities were also consistent with TROPOMI's coarser spatial resolution and documented TROPOMI biases, with columns biased low under polluted conditions (high NO$_2$) and biased high at low NO$_2$ levels, which have been attributed to the lower resolution surface albedo characterization (0.5° OMI LER) and the coarse resolution of the TM5-MP a priori profiles used in the standard product.[77,80] While a similar analysis for TROPOMI has not yet been published, McLinden et al.[81] found that a custom high-resolution OMI retrieval reduced the AMF over NO$_2$ plumes compared to the DOMINOv2 (similar to the retrieval used here) where the vertical column is equal to the slant column/AMF. The ratio of the custom retrieval AMF to the DOMINOv2 AMF was maximal at 1.9 over the NO$_x$ source but decreased to 1 on a spatial scale relevant to an urban−suburban gradient, and, as a result, TROPOMI observations likely underestimate the severity of NO$_2$

disparities. That being said, we have found that annually averaged TROPOMI maps do capture a key portion of LIN-HIW differences (and inequality by other metrics) compared to those from GCAS despite the effects of temporal averaging and biases.

TROPOMI and afternoon GCAS measurements were compared as joint probability density functions of household income and fractional census tract race-ethnicity sorted into the lowest (0−20% of the NO_2 column distribution), intermediate (40−60%), and highest-NO_2 (80−100%) quintiles; Figure 4 shows the median contours of each density
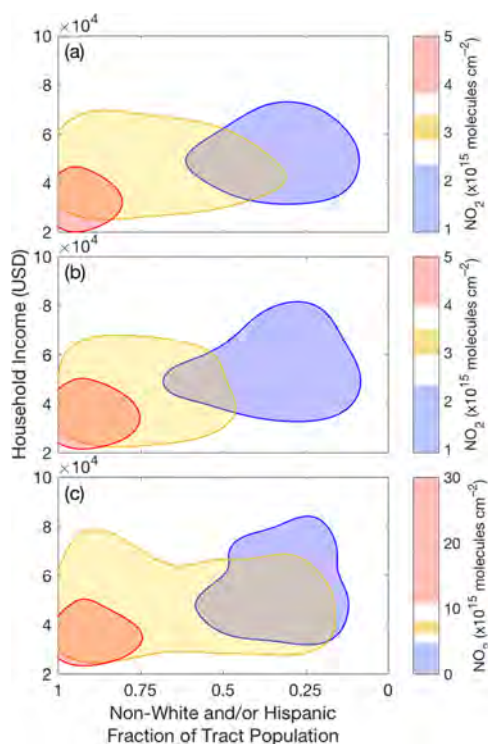

Figure 4. HMA population as a function of census tract annual household income (USD) and non-white/Hispanic or non-Hispanic white fractions separated by a census-tract-averaged NO_2 column quintile: high NO_2 (80−100% highest column densities) (red), mid-quintile NO_2 (40−60%) (yellow), and low NO_2 (0−20%) (blue). (a, b) Annual (June 2018 to May 2019) weekday (Tuesday−Friday) TROPOMI observations across the HMA (a) and along the GCAS flight track (b). (c) Composite distribution of all 35 GCAS circuits. Color bars represent vertical column densities (molecules cm^{-2}) corresponding to the NO_2 quintiles.

function. The results showed that neighborhood-level differences were not driven by outliers but represented broader patterns in the NO_2 distribution with neighborhood demographics. TROPOMI and GCAS described similar patterns: low NO_2 census tracts were more likely to be white and of higher income, and intermediate and high NO_2 tracts were more likely to be non-white, Hispanic, and of low income. Figure 4 also illustrates that TROPOMI and GCAS represented the NO_2 column density distributions as normal or log-normal, respectively (represented in the color scales), which was consistent with the coarser spatial resolution of the TROPOMI observations and their reported low bias at high NO_2. In addition, while the high (red) and low (blue) quintiles were comparable between datasets, there was more variation in

the mid (yellow) quintile, reflective of these differences in the NO_2 distribution.

Finally, census tracts are aspatial administrative units optimally sized around 4000 people that represent fine spatial scales in cities. In Houston's "urbanized areas" (Figure S15), census tracts were on average 4.7 ± 6.5 km^2 (∼2 km × 2 km if square) and the smallest 20% of tracts were on average 1.2 ± 0.3 km^2. Because the smallest tracts are the size of our oversampled TROPOMI product resolution, finer-scale analyses are likely limited. On average, the even smaller administrative unit of the U.S. Census block group, optimally sized at ∼1500 people, was 2.1 ± 5.5 km^2 in the "urbanized areas" and just 0.3 ± 0.1 km^2 in the smallest 20% of tracts with the latter approaching the limit of the GCAS spatial resolution. At the block-group level, we computed LIN-HIW NO_2 differences of 22 ± 5% for TROPOMI and 30 ± 4% for GCAS (all circuits), which were 35% and 17% lower than computed at the tract level, respectively, suggesting even the GCAS resolution was too coarse to fully resolve block-group-scale disparities. While finer-scale data hypothetically reveal greater NO_2 inhomogeneity and inequality, higher-resolution NO_2 remote sensing observations potentially underestimate the impacts of NO_x emissions. Because NO_x is primarily emitted as NO and then converted to NO_2 in the presence of ozone, NO_2 remote sensing misses the portion of NO_2 temporarily stored as NO as the system reaches steady state. This is important for a city-wide NO_2 column comparison in differently sized tracts, especially if using NO_2 as a surrogate for other co-emitted species, as sources are more prevalent in low-income neighborhoods, non-white and Hispanic residents are statistically overrepresented in tracts with higher population densities, and ozone concentrations are spatially variable.

NO_2 Column-Surface Relationships. Satellite and sub-orbital remote sensing instruments observe NO_2 columns and precisely capture surface neighborhood-scale differences when NO_2 vertical distributions do not co-vary with census-tract demographics. Daytime continental NO_2 mixing ratios are typically highest within the convective boundary layer (CBL), the thin layer of air in contact with the Earth's surface. While long-lived species are generally well-mixed in the CBL, NO_2 can exhibit steeper vertical gradients, as chemical loss and turbulent mixing timescales are similar.[82] To investigate the extent that NO_2 columns represented surface-level patterns in tract-scale NO_2 inequality, not the surface concentrations themselves, which is a key factor in their application to air pollution decision making, we analyzed spatiotemporal variability in in situ NO_2 vertical profiles and TROPOMI columns to NO_2* surface measurements.

As part of DISCOVER-AQ, the NASA P-3B aircraft profiled the lower troposphere, spanning altitudes of 3−0.3 km at locations corresponding to the GCAS flight path (Figure S16). In their detailed evaluation of the GCAS retrieval during DISCOVER-AQ, Nowlan et al. showed that observations from GCAS and aircraft profiling were well correlated with an overall r^2 of 0.89. We focus on 144 profiles representing tracts of varied population demographics in downtown (Moody Tower), the HSC (Channelview and Deer Park), and suburban Houston (Conroe, West Houston, and Manvel Croix), collected on eight weekdays in the morning (8:30−10:30 am, LT), at midday (11:30 am−1 pm, LT), and in the afternoon (1:30−3:30, LT) (Figure S13). Profiling at Deer Park, Conroe, and West Houston included missed approaches

over lightly trafficked air strips, facilitating sampling below altitudes of 0.1 km. All profiles are provided in the Supporting Information.

CBL heights were on average 0.8 ± 0.2 km ($\pm 1\sigma$) in the morning, 1.5 ± 0.5 km at midday, and 1.7 ± 0.6 km in the afternoon. CBL heights were not statistically different at any profile location, and temporal variability was generally well correlated across sites (Table S2). In the morning, the slope of the correlation between the 3 km column and within-CBL column (Table S4 and Figure S17) was 0.80 ± 0.18 ($r^2 = 0.99$), and, once the CBL was fully developed (midday and afternoon), the slope was 0.98 ± 0.15 ($r^2 = 0.99$). The slope of correlation between the column within the CBL and below 500 m AGL was 0.83 ± 0.19 ($r^2 = 0.95$) in the morning. Once the CBL was developed, the slope decreased to 0.27 ± 0.05 ($r^2 = 0.80$), consistent with atmospheric conditions in which timescales of turbulent mixing and NO_2 chemical loss are competitive. The high correlation coefficients indicated that location-dependent differences in the NO_2 vertical distribution were small and demographic-based NO_2 comparisons would not substantially differ if derived from surface measurements instead of columns.

We then compared tract-averaged TROPOMI columns and daytime (12−3 pm LT) NO_2* surface mixing ratios measured at monitors across the HMA (Figure 5). We linearly correlated
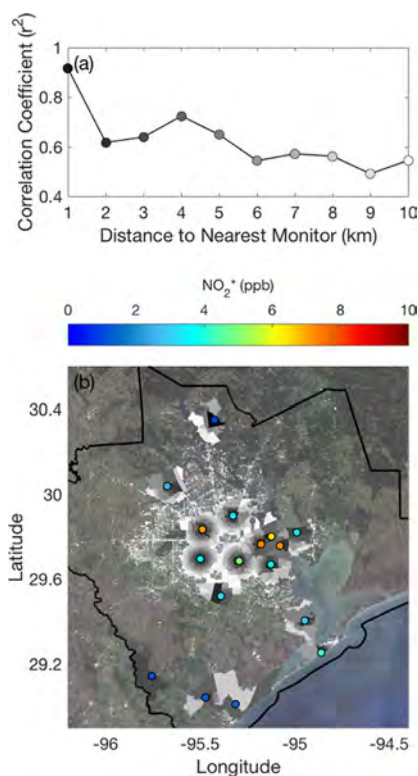

Figure 5. (a) Correlation coefficient between tract-averaged NO_2 measured at surface monitors and their overhead columns as a function of distance away from the monitor with respect to the census tract center point. NO_2* observations are daytime (12−3 pm LT) averages and both datasets include weekdays (Tuesday−Friday) over June 2018 to May 2019. (b) Census tracts coloration indicates the distance (km) between the nearest surface NO_2 monitoring station and the census tract center point for tracts within a 10 km radius. Background map data: Landsat 8 composite over January 2017 to June 2018.

annual (June 2018 to May 2019) weekday (Tuesday−Friday) mean observations as a function of the distance between tract center points and the nearest monitors. Surface NO_2* and directly overhead columns (tracts within 1 km of monitors) were strongly correlated ($r^2 = 0.92$). However, r^2 decreased with increasing distance from the nearest monitor, falling to 0.63−0.75 when tracts were 2−5 km from the local monitor and 0.50−0.58 at distances of 5−10 km. Column-surface correlations have also been shown to improve with monitor density elsewhere using simulated TROPOMI datasets[36] and observations from the more coarsely resolved satellite OMI sensor.[31] While an evaluation of the daily TROPOMI observations is the subject of a future manuscript, we investigated the temporal correlation between individual daytime (12−3 pm LT) mean surface NO_2* mixing ratios and overhead (within 1 km of a monitoring station) annual weekday TROPOMI NO_2 columns (Figure 3b). The mean correlation coefficient, including days when at least 75% of monitoring stations were operational, was 0.66 ± 0.17 (see Figure S14 for histograms of the individual values) with no significant seasonal variation observed. While further analysis would have been required to infer surface concentrations, our results showed that TROPOMI captured typical NO_2 surface patterns, and, therefore, surface-level NO_2 inequality, but the use of annual average TROPOMI observations obscured day-to-day variability in the surface NO_2 distribution. The steep decline in r^2 at 1−2 km corresponded to previously observed NO_2 distance-decay gradients,[29,30] demonstrating the limits of the routine network to detect representative NO_2 levels for the majority of local residents, an advantage of TROPOMI, as just 3.4% of census tracts in the HMA (based on tract center points) were located within 2 km of a NO_2 monitor.

NO_x Source Contributions to Census-Tract NO_2 Differences. To investigate the greater temporal variability in the GCAS results and observationally evaluate the contribution of heavy-duty diesel trucking emissions to inequality, we analyzed LIN-HIW differences reported in the FIVE and stationary source NEI using the same population weighting applied to the NO_2 column observations. Total population-weighted emission densities (metric tons NO_2-eq day^{-1} km^{-2}) (composed of on-road diesel and gasoline-powered vehicles, industrial and petrochemical facilities, and electricity generation) were 5 times higher for LINs than for HIWs. Gasoline-powered and heavy-duty diesel vehicle (HDDV) emission densities were 4 and 4.2 times greater for LINs than for HIWs, respectively. The largest disparities were found for industrial sources with 10 times greater emission densities for LINs than for HIWs. This unequal distribution of emission sources was consistent with our observation or more variable NO_2 concentrations and our inference of greater NO_x emissions in proximity to non-white, Hispanic, and low-income households.

Satellite remote sensing has the advantage of capturing temporal variability useful for interpreting the impact of NO_x sources, in particular, NO_2 differences on weekdays and weekends that are driven largely by HDDV traffic patterns.[35,67] HDDVs represent just 3−6% of the number vehicles in the U.S. vehicle fleet; however, because diesel engines produce ∼7 times more NO_x per kilogram of fuel burned than gasoline,[72] they contribute a substantial portion of NO_x emissions in many U.S cities.[73] HDDVs have been shown to contribute to air pollution disparities in multiple U.S. cities,[83−87] and their exhaust has been associated with a myriad of adverse health

effects.[18] Because HDDVs transport commercial goods, their emissions are reduced on weekends.[35,88] At the same time, passenger vehicle traffic and point source NO_x emissions do not exhibit similarly significant weekday−weekend decreases,[83,89] although the timing of these emissions shift with greater weekend traffic outside of rush hour at midday.[89]

To evaluate the influence of HDDV emissions on NO_2 column observations, we compared annual weekday (Tuesday−Friday) and weekend (Saturday−Sunday) tract-level population-weighted TROPOMI NO_2 measurements (Figure 2b,c). NO_2 columns unweighted by population were 29% lower on weekends than on weekdays with weekend NO_2 column enhancements primarily near the HSC and western shore of Galveston Bay (Figure 3c) where industrial sources in the HMA are concentrated. We calculated greater weekend NO_2 decreases for LINs ($24 \pm 2\%$) than for HIWs ($15 \pm 2\%$). If HDDV traffic caused the entire weekday−weekend difference, then HDDV emissions contributed $25 \pm 3\%$ of the LIN-HIW population-weighted NO_2 column inequality across Houston. The same calculation based on inventory data produced weekday−weekend differences of $22 \pm 2\%$ with the slight variance compared to the observations, potentially due to co-varying gasoline vehicle traffic patterns and/or changes in the NO_2 chemical lifetime. Comparable results between TROPOMI and FIVE + NEI, at least in the HMA, are in part due to the uniquely high spatial resolution of the FIVE inventory (500 m × 500 m); for example, standard NEI emission files (that include mobile sources) are 4 km × 4 km, typically too coarse to resolve traffic emissions along highways.[90] TROPOMI may therefore be suited to inform NO_2 inequality analyses in cities with incomplete, uncertain, out-of-date, and/or poorly-resolved (in space and time) inventories.

Conclusions and Looking Forward. We quantified the unequal distribution of NO_2 across the city of Houston using high spatial resolution GCAS airborne observations (250 m × 500 m), which were fine enough to resolve census-tract-scale NO_2 spatial variability. During DISCOVER-AQ, we found that population-weighted NO_2 was $37 \pm 6\%$ higher for non-whites and Hispanics living in low-income tracts compared to whites living in high-income tracts; additionally, there were NO_2 disparities of 11−32% by race-ethnicity and 15−28% by poverty status. We used this analysis as a basis of comparison to determine that TROPOMI resolved similar tract-level NO_2 disparities. We observed that, while population-weighted GCAS NO_2 columns were always greater for non-white, Hispanic, and low-income residents, they were also substantially more temporally variable, a consequence of the higher NO_x source density in these neighborhoods. Greater temporal variability has implications for research on the acute health impacts of NO_2, and its surrogates, for LINs, as time-averaged pollutant data and static LUR models do not represent high NO_2 events, such as that observed on September 25 and reflected in the shift in the NO_2 column statistical distribution from log-normal (GCAS, 35 flight circuits) to normal (TROPOMI, one year of weekends) (Figure 4). Because long-term averaging does not inherently change the underlying data distribution and given that TROPOMI has at least the potential for daily coverage, the impact of transient extreme events could still be captured by analyzing other aspects of the NO_2 column distribution. In addition, the multiyear time record of the TROPOMI and ongoing data collection provide empirical evidence of specific time-varying NO_x source

contributions potentially relevant for political and regulatory decision making; for example, weekday−weekend NO_2 differences in Houston indicate that HDDVs cause up to 25% of the city's NO_2 disparities. Such information can be used by city planners, elected officials, and other decision makers as they develop comprehensive plans, allocate resources for mitigation, invest in public transportation, and/or implement vehicle bans.

Spatially and temporally extensive air quality observations are foundational for successful policy design, implementation, and evaluation in every city, especially for controversial issues like environmental justice; this is because they can reduce uncertainties about the severity of disparities for specific chemicals, which are often at the root of related policy disputes. Here, we demonstrated that TROPOMI (over-sampled to 0.01° × 0.01°) precisely observes NO_2 differences between census tracts and the spatial patterns in NO_2 columns reflect those measured at the surface. However, our results also suggested that TROPOMI-derived NO_2 disparities generally represent lower bounds with time averaging needed to improve measurement spatial resolution and documented retrieval biases that minimize absolute NO_2 differences. Still, TROPOMI measurements may be well positioned to inform multiple aspects of city-wide decision making in novel ways, for example, in the development of local interventions, such as ordinances, moratoriums, comprehensive plans, zoning, siting decisions, traffic planning, and permitting; through data-driven regulatory enforcement; and by supporting resource prioritization for environmental equity, especially in areas lacking surface monitoring. Because NO_x partitioning favors NO in the nearfield of sources, which are more prevalent in non-white, Hispanic, and low-income neighborhoods, at least in Houston, broader application of satellite NO_2 columns as a surrogate for toxic combustion emissions requires further consideration. Even so, the TROPOMI observations have the potential to promote targeted and tailored municipal NO_x intervention efforts, illuminate limitations to cities' enforcement capacities (e.g., growth in road transport), and inform policies to ensure compliance and equitable outcomes. Finally, the geostationary satellite TEMPO instrument (planned launch date in 2022) will provide hourly column observations of up to 2 km × 4.5 km at the center of its field of regard over North America, resulting in the most spatially and temporally precise space-based NO_2 observations over the United States to date.[91] Finer city-wide spatiotemporal details will further expand our ability to reveal, document, and monitor census-tract-level NO_2 disparities to observe high-NO_2 events, infer source contributions from temporal variability, and inform decision making to eliminate the practices, behaviors, and conditions contributing to racial, ethnic, and income-based air quality disparities in major U.S. cities.

■ ASSOCIATED CONTENT

ⓈI Supporting Information

The Supporting Information is available free of charge at https://pubs.acs.org/doi/10.1021/acs.est.0c01864.

> Study area maps, individual GCAS circuit NO_2 maps, surface wind statistics on GCAS flight days, temporal trends in surface NO_2*, TROPOMI columns sub-sampled along the GCAS track, NASA P-3B flight path and profile, CBL and in situ NO_2 column statistics, and

all individual measured NO$_2$, theta lapse rate, theta, and H$_2$O$_{(v)}$ profiles (Figures S15−S63) (PDF)

AUTHOR INFORMATION

Corresponding Author

Sally E. Pusede − *Department of Environmental Sciences, University of Virginia, Charlottesville, Virginia 22904, United States;* orcid.org/0000-0002-3041-0209; Email: sepusede@virginia.edu

Authors

Mary Angelique G. Demetillo − *Department of Environmental Sciences, University of Virginia, Charlottesville, Virginia 22904, United States;* orcid.org/0000-0002-0618-9022

Aracely Navarro − *Department of Public Health, Emory University, Atlanta, Georgia 30322, United States*

Katherine K. Knowles − *Department of Environmental Sciences, University of Virginia, Charlottesville, Virginia 22904, United States*

Kimberly P. Fields − *Carter G. Woodson Institute for African-American and African Studies, University of Virginia, Charlottesville, Virginia 22904, United States*

Jeffrey A. Geddes − *Department of Earth and Environment, Boston University, Boston, Massachusetts 02215, United States;* orcid.org/0000-0001-7573-6133

Caroline R. Nowlan − *Atomic and Molecular Physics Division, Harvard Smithsonian Center for Astrophysics, Cambridge, Massachusetts 02138, United States*

Scott J. Janz − *NASA Goddard Space Flight Center, Greenbelt, Maryland 20771, United States*

Laura M. Judd − *NASA Langley Research Center, Hampton, Virginia 23681, United States*

Jassim Al-Saadi − *NASA Langley Research Center, Hampton, Virginia 23681, United States*

Kang Sun − *Department of Civil, Structural and Environmental Engineering and Research and Education in eNergy, Environment and Water (RENEW) Institute, University at Buffalo, New York 14260, United States*

Brian C. McDonald − *Cooperative Institute for Research in Environmental Sciences, University of Colorado, Boulder, Colorado 80305, United States; Chemical Sciences Division, NOAA Earth System Research Laboratory, Boulder, Colorado 80305, United States;* orcid.org/0000-0001-8600-5096

Glenn S. Diskin − *NASA Langley Research Center, Hampton, Virginia 23681, United States*

Complete contact information is available at:
https://pubs.acs.org/10.1021/acs.est.0c01864

Notes

The authors declare no competing financial interest.
Data files of GCAS and TROPOMI observations averaged to census tracts are available for download at https://pusede.evsc.virginia.edu/home/data/.

REFERENCES

(1) *State of the Air 2019*; American Lung Association: April 24, 2019.
(2) *National Air Toxics Assessment 2014*; U.S. Environmental Protection Agency, 2014.
(3) Collins, T. W.; Grineski, S. E.; Chakraborty, J.; Montgomery, M. C.; Hernandez, M. Downscaling Environmental Justice Analysis: Determinants of Household-Level Hazardous Air Pollutant Exposure in Greater Houston. *Ann. Am. Assoc. Geogr.* 2015, 105, 684−703.
(4) Hernandez, M.; Collins, T. W.; Grineski, S. E. Immigration, mobility, and environmental injustice: A comparative study of Hispanic people's residential decision-making and exposure to hazardous air pollutants in Greater Houston, Texas. *Geoforum* 2015, 60, 83−94.
(5) Bullard, R. D. *Invisible Houston: the Black experience in boom and bust*; Texas A & M University Press: College Station, 1987.
(6) Linder, S. H.; Marko, D.; Sexton, K. Cumulative Cancer Risk from Air Pollution in Houston: Disparities in Risk Burden and Social Disadvantage. *Environ. Sci. Technol.* 2008, 42, 4312−4322.
(7) Sansom, G.; Parras, J.; Parras, A.; Nieto, Y.; Arellano, Y.; Berke, P.; McDonald, T.; Shipp, E.; Horney, J. A. The Impacts of Exposure to Environmental Risk on Physical and Mental Health in a Small Geographic Community in Houston, TX. *J. Community Health* 2017, 42, 813−818.
(8) Clark, L. P.; Millet, D. B.; Marshall, J. D. Changes in Transportation-Related Air Pollution Exposures by Race-Ethnicity and Socioeconomic Status: Outdoor Nitrogen Dioxide in the United States in 2000 and 2010. *Environ. Health Perspect.* 2017, 125, 097012.
(9) Clark, L. P.; Millet, D. B.; Marshall, J. D. National Patterns in Environmental Injustice and Inequality: Outdoor NO$_2$ Air Pollution in the United States. *PLoS One* 2014, 9, No. e94431.
(10) Levy, I.; Mihele, C.; Lu, G.; Narayan, J.; Brook, J. R. Evaluating Multipollutant Exposure and Urban Air Quality: Pollutant Inter-relationships, Neighborhood Variability, and Nitrogen Dioxide as a Proxy Pollutant. *Environ. Health Perspect.* 2014, 122, 65−72.
(11) Jerrett, M.; Burnett, R. T.; Ma, R.; Pope, C. A., III; Krewski, D.; Newbold, K. B.; Thurston, G.; Shi, Y.; Finkelstein, N.; Calle, E. E.; Thun, M. J. Spatial analysis of air pollution and mortality in Los Angeles. *Epidemiology* 2005, 16, 727.
(12) Morello-Frosch, R.; Jesdale, B. M. Separate and unequal: residential segregation and estimated cancer risks associated with ambient air toxics in U.S. metropolitan areas. *Environ. Health Perspect.* 2006, 114, 386−393.
(13) Hajat, A.; Hsia, C.; O'Neill, M. S. Socioeconomic Disparities and Air Pollution Exposure: a Global Review. *Curr. Environ. Health Rep.* 2015, 2, 440−450.
(14) *Profile of version 1 of the 2014 National Emissions Inventory*; Office of Air Quality Planning and Standards, Emissions Inventory and Analysis Group: April, 2017.
(15) Kim, S.-W.; McKeen, S. A.; Frost, G. J.; Lee, S.-H.; Trainer, M.; Richter, A.; Angevine, W. M.; Atlas, E.; Bianco, L.; Boersma, K. F.; Brioude, J.; Burrows, J. P.; de Gouw, J.; Fried, A.; Gleason, J. F.; Hilboll, A.; Mellqvist, J.; Peischl, J.; Richter, D.; Rivera, C.; Ryerson, T.; te Lintel Hekkert, S.; Walega, J.; Warneke, C.; Weibring, P.; Williams, E. Evaluations of NO$_x$ and highly reactive VOC emission inventories in Texas and their implications for ozone plume simulations during the Texas Air Quality Study 2006. *Atmos. Chem. Phys.* 2011, 11, 11361−11386.
(16) Rivera, C.; Mellqvist, J.; Samuelsson, J.; Lefer, B.; Alvarez, S.; Patel, M. R. Quantification of NO$_2$ and SO$_2$ emissions from the Houston Ship Channel and Texas City industrial areas during the 2006 Texas Air Quality Study. *J. Geophys. Res.: Atmos.* 2010, 27, D08301.

(17) Washenfelder, R. A.; Trainer, M.; Frost, G. J.; Ryerson, T. B.; Atlas, E. L.; de Gouw, J. A.; Flocke, F. M.; Fried, A.; Holloway, J. S.; Parrish, D. D.; Peischl, J.; Richter, D.; Schauffler, S. M.; Walega, J. G.; Warneke, C.; Weibring, P.; Zheng, W. Characterization of NO_x, SO_2, ethene, and propene from industrial emission sources in Houston, Texas. *J. Geophys. Res.: Atmos.* **2010**, *115*, D16311.

(18) *Traffic-Related Air Pollution: A Critical Review of the Literature on Emissions, Exposure, and Health Effects*; Health Effects Institute, 2010, (Special Report 17).

(19) Brook, J. R.; Burnett, R. T.; Dann, T. F.; Cakmak, S.; Goldberg, M. S.; Fan, X.; Wheeler, A. J. Further interpretation of the acute effect of nitrogen dioxide observed in Canadian time-series studies. *J. Exposure Sci. Environ. Epidemiol.* **2007**, *17*, S36–S44.

(20) Brunekreef, B.; Holgate, S. T. Air pollution and health. *Lancet* **2002**, *360*, 1233–1242.

(21) Burnett, R. T.; Stieb, D.; Brook, J. R.; Cakmak, S.; Dales, R.; Raizenne, M.; Vincent, R.; Dann, T. Associations between short-term changes in nitrogen dioxide and mortality in Canadian cities. *Arch. Environ. Health* **2004**, *59*, 228–236.

(22) Crouse, D. L.; Peters, P. A.; Hystad, P.; Brook, J. R.; van Donkelaar, A.; Martin, R. V.; Villeneuve, P. J.; Jerrett, M.; Goldberg, M. S.; Pope, C. A., III; Brauer, M.; Brook, R. D.; Robichaud, A.; Menard, R.; Burnett, R. T. Ambient $PM_{2.5}$, O_3, and NO_2 Exposures and Associations with Mortality over 16 Years of Follow-Up in the Canadian Census Health and Environment Cohort (CanCHEC). *Environ. Health Perspect.* **2015**, *123*, 1180–1186.

(23) Edwards, J.; Walters, S.; Griffiths, R. K. Hospital Admissions for Asthma in Preschool-Children - Relationship to Major Roads in Birmingham, United-Kingdom. *Arch. Environ. Health* **1994**, *49*, 223–227.

(24) Gauderman, W. J.; Avol, E.; Lurmann, F.; Kuenzli, N.; Gilliland, F.; Peters, J.; McConnell, R. Childhood asthma and exposure to traffic and nitrogen dioxide. *Epidemiology* **2005**, *16*, 737–743.

(25) Lin, S.; Munsie, J. P.; Hwang, S. A.; Fitzgerald, E.; Cayo, M. R. Childhood asthma hospitalization and residential exposure to state route traffic. *Environ. Res.* **2002**, *88*, 73–81.

(26) Adar, S. D.; Kaufman, J. D. Cardiovascular disease and air pollutants: Evaluating and improving epidemiological data implicating traffic exposure. *Inhalation Toxicol.* **2007**, *19*, 135–149.

(27) Lipfert, F. W.; Wyzga, R. E. On exposure and response relationships for health effects associated with exposure to vehicular traffic. *J. Exposure Sci. Environ. Epidemiol.* **2008**, *18*, 588–599.

(28) Wu, J.; Ren, C.; Delfino, R. J.; Chung, J.; Wilhelm, M.; Ritz, B. Association between Local Traffic-Generated Air Pollution and Preeclampsia and Preterm Delivery in the South Coast Air Basin of California. *Environ. Health Perspect.* **2009**, *117*, 1773–1779.

(29) Choi, W.; He, M.; Barbesant, V.; Kozawa, K. H.; Mara, S.; Winer, A. M.; Paulson, S. E. Prevalence of wide area impacts downwind of freeways under pre-sunrise stable atmospheric conditions. *Atmos. Environ.* **2012**, *62*, 318–327.

(30) Karner, A. A.; Eisinger, D. S.; Niemeier, D. A. Near-Roadway Air Quality: Synthesizing the Findings from Real-World Data. *Environ. Sci. Technol.* **2010**, *44*, 5334–5344.

(31) Bechle, M. J.; Millet, D. B.; Marshall, J. D. Remote sensing of exposure to NO_2: Satellite versus ground-based measurement in a large urban area. *Atmos. Environ.* **2013**, *69*, 345–353.

(32) Rowangould, G. M. A census of the US near-roadway population: Public health and environmental justice considerations. *Trans. Res. D Trans. Environ.* **2013**, *25*, 59–67.

(33) Boersma, K. F.; Jacob, D. J.; Trainic, M.; Rudich, Y.; DeSmedt, I.; Dirksen, R.; Eskes, H. J. Validation of urban NO_2 concentrations and their diurnal and seasonal variations observed from the SCIAMACHY and OMI sensors using in situ surface measurements in Israeli cities. *Atmos. Chem. Phys.* **2009**, *9*, 3867–3879.

(34) Geddes, J. A.; Martin, R. V.; Boys, B. L.; van Donkelaar, A. Long-Term Trends Worldwide in Ambient NO_2 Concentrations Inferred from Satellite Observations. *Environ. Health Perspect.* **2016**, *124*, 281–289.

(35) Russell, A. R.; Valin, L. C.; Cohen, R. C. Trends in OMI NO_2 Observations over the United States: Effects of Emission Control Technology and the Economic Recession. *Atmos. Chem. Phys.* **2012**, *12*, 12197–12209.

(36) Judd, L. M.; Al-Saadi, J. A.; Janz, S. J.; Kowalewski, M. G.; Pierce, R. B.; Szykman, J. J.; Valin, L. C.; Swap, R.; Cede, A.; Mueller, M.; Tiefengraber, M.; Abuhassan, N.; Williams, D. Evaluating the impact of spatial resolution on tropospheric NO_2 column comparisons within urban areas using high-resolution airborne data. *Atmos. Meas. Tech.* **2019**, *12*, 6091–6111.

(37) Valin, L. C.; Russell, A. R.; Bucsela, E. J.; Veefkind, J. P.; Cohen, R. C. Observation of slant column NO_2 using the super-zoom mode of AURA-OMI. *Atmos. Meas. Tech.* **2011**, *4*, 1929–1935.

(38) Larkin, A.; Geddes, J. A.; Martin, R. V.; Xiao, Q.; Liu, Y.; Marshall, J. D.; Brauer, M.; Hystad, P. Global Land Use Regression Model for Nitrogen Dioxide Air Pollution. *Environ. Sci. Technol.* **2017**, *51*, 6957–6964.

(39) Novotny, E. V.; Bechle, M. J.; Millet, D. B.; Marshall, J. D. National Satellite-Based Land-Use Regression: NO_2 in the United States. *Environ. Sci. Technol.* **2011**, *45*, 4407–4414.

(40) Su, J. G.; Jerrett, M.; Beckerman, B.; Wilhelm, M.; Ghosh, J. K.; Ritz, B. Predicting traffic-related air pollution in Los Angeles using a distance decay regression selection strategy. *Environ. Res.* **2009**, *109*, 657–670.

(41) Nowlan, C. R.; Liu, X.; Janz, S. J.; Kowalewski, M. G.; Chance, K.; Follette-Cook, M. B.; Fried, A.; González Abad, G.; Herman, J. R.; Judd, L. M.; Kwon, H.-A.; Loughner, C. P.; Pickering, K. E.; Richter, D.; Spinei, E.; Walega, J.; Weibring, P.; Weinheimer, A. J. Nitrogen dioxide and formaldehyde measurements from the GEOstationary Coastal and Air Pollution Events (GEO-CAPE) Airborne Simulator over Houston, Texas. *Atmos. Meas. Tech.* **2018**, *11*, 5941–5964.

(42) Nowlan, C. R.; Liu, X.; Leitch, J. W.; Chance, K.; González Abad, G.; Liu, C.; Zoogman, P.; Cole, J.; Delker, T.; Good, W.; Murcray, F.; Ruppert, L.; Soo, D.; Follette-Cook, M. B.; Janz, S. J.; Kowalewski, M. G.; Loughner, C. P.; Pickering, K. E.; Herman, J. R.; Beaver, M. R.; Long, R. W.; Szykman, J. J.; Judd, L. M.; Kelley, P.; Luke, W. T.; Ren, X.; Al-Saadi, J. A. Nitrogen dioxide observations from the Geostationary Trace gas and Aerosol Sensor Optimization (GeoTASO) airborne instrument: Retrieval algorithm and measurements during DISCOVER-AQ Texas 2013. *Atmos. Meas. Tech.* **2016**, *9*, 2647–2668.

(43) Souri, A. H.; Choi, Y.; Pan, S.; Curci, G.; Nowlan, C. R.; Janz, S. J.; Kowalewski, M. G.; Liu, J.; Herman, J. R.; Weinheimer, A. J. First Top-Down Estimates of Anthropogenic NOx Emissions Using High-Resolution Airborne Remote Sensing Observations. *J. Geophys. Res.: Atmos.* **2018**, *123*, 3269–3284.

(44) U.S. Census Burea, P. D. *Annual Estimates of Resident Population*. April 1, 2010 to July 1, 2018. https://factfinder.census.gov/faces/tableservices/jsf/pages/productview.xhtml?src=bkmk (accessed August 1).

(45) *Texas State Energy Profile.* https://www.eia.gov/state/print.php?sid=TX (accessed October 7, 2019).

(46) *Senate Select Committee on Texas Ports. Overview of Texas Ports and Waterways*; May 3, 2016, 2016.

(47) Darby, L. S. Cluster Analysis of Surface Winds in Houston, Texas, and the Impact of Wind Patterns on Ozone. *J. Appl. Meteorol.* **2005**, *44*, 1788–1806.

(48) *State of Global Air 2019*; Health Effects Institute, Boston, *MA*, 2019.

(49) Sexton, K.; Linder, S. H.; Marko, D.; Bethel, H.; Lupo, P. J. Comparative assessment of air pollution-related health risks in Houston. *Environ. Health Perspect.* **2007**, *115*, 1388–1393.

(50) Leitch, J. W. D. T.; Good, W.; Ruppert, L.; Murcray, F.; Chance, K.; Liu, X.; Nowlan, C.; Janz, S. J.; Krotkov, N. A.; Pickering, K. E.; Kowalewski, M.; Wang, J. The GeoTASO airborne spectrometer project. In *Earth Observing Systems*; International Society for Optics and Photonics, p 9., 2014.

(51) Skamarock, W. C.; Klemp, J. B.; Dudhia, J.; Gill, D. O.; Barker, D. M.; Duda, M. G.; Huang, X.-Y.; Wang, W.; Powers, J. G. *A*

Description of the Advanced Research WRF Version 3; University Corporation for Atmospheric Research: Boulder, Colorado, 2008.

(52) Otte, T. L.; Pleim, J. E. The Meteorology-Chemistry Interface Processor (MCIP) for the CMAQ modeling system: updates through MCIPv3.4.1. *Geosci. Model Dev.* **2010**, *3*, 243−256.

(53) Loughner, C. P.; Follette-Cook, M. *Emission source region contributions to a high surface ozone episode during DISCOVER-AQ, final Report to Texas AQRP*; 2015.

(54) van Geffen, J. H. G.; Boersma, K. F.; Eskes, H. J.; Maasakkers, J. D.; Veefkind, J. P. *TROPOMI ATBD of the total and tropospheric NO2 data products*. http://www.tropomi.eu (accessed 12 May).

(55) Veefkind, J. P.; Aben, I.; McMullan, K.; Förster, H.; de Vries, J.; Otter, G.; Claas, J.; Eskes, H. J.; de Haan, J. F.; Kleipool, Q.; van Weele, M.; Hasekamp, O.; Hoogeveen, R.; Landgraf, J.; Snel, R.; Tol, P.; Ingmann, P.; Voors, R.; Kruizinga, B.; Vink, R.; Visser, H.; Levelt, P. F. TROPOMI on the ESA Sentinel-5 Precursor: A GMES mission for global observations of the atmospheric composition for climate, air quality and ozone layer applications. *Remote Sens. Environ.* **2012**, *120*, 70−83.

(56) Boersma, K. F.; Eskes, H. J.; Dirksen, R. J.; van der A, R. J.; Veefkind, J. P.; Stammes, P.; Huijnen, V.; Kleipool, Q. L.; Sneep, M.; Claas, J.; Leitao, J.; Richter, A.; Zhou, Y.; Brunner, D. An improved tropospheric NO$_2$ column retrieval algorithm for the Ozone Monitoring Instrument. *Atmos. Meas.Tech.* **2011**, *4*, 1905−1928.

(57) Lorente, A.; Folkert Boersma, K.; Yu, H.; Dörner, S.; Hilboll, A.; Richter, A.; Liu, M.; Lamsal, L. N.; Barkley, M.; De Smedt, I.; Van Roozendael, M.; Wang, Y.; Wagner, T.; Beirle, S.; Lin, J. T.; Krotkov, N.; Stammes, P.; Wang, P.; Eskes, H. J.; Krol, M. Structural uncertainty in air mass factor calculation for NO$_2$ and HCHO satellite retrievals. *Atmos. Meas. Tech.* **2017**, *10*, 759−782.

(58) van Geffen, J. H. G. M.; Boersma, K. F.; Van Roozendael, M.; Hendrick, F.; Mahieu, E.; De Smedt, I.; Sneep, M.; Veefkind, J. P. Improved spectral fitting of nitrogen dioxide from OMI in the 405−465 nm window. *Atmos. Meas. Tech.* **2015**, *8*, 1685−1699.

(59) Zara, M.; Boersma, K. F.; De Smedt, I.; Richter, A.; Peters, E.; van Geffen, J. H. G. M.; Beirle, S.; Wagner, T.; Van Roozendael, M.; Marchenko, S.; Lamsal, L. N.; Eskes, H. J. Improved slant column density retrieval of nitrogen dioxide and formaldehyde for OMI and GOME-2A from QA4ECV: intercomparison, uncertainty characterisation, and trends. *Atmos. Meas. Tech.* **2018**, *11*, 4033−4058.

(60) Boersma, K. F.; Eskes, H. J.; Richter, A.; De Smedt, I.; Lorente, A.; Beirle, S.; van Geffen, J. H. G. M.; Zara, M.; Peters, E.; Van Roozendael, M.; Wagner, T.; Maasakkers, J. D.; van der A, R. J.; Nightingale, J.; De Rudder, A.; Irie, H.; Pinardi, G.; Lambert, J. C.; Compernolle, S. C. Improving algorithms and uncertainty estimates for satellite NO$_2$ retrievals: results from the quality assurance for the essential climate variables (QA4ECV) project. *Atmos. Meas.Tech.* **2018**, *11*, 6651−6678.

(61) Boersma, K. F.; Eskes, H. J.; Brinksma, E. J. Error analysis for tropospheric NO$_2$ retrieval from space. *J. Geophys. Res.: Atmos.* **2004**, *109*, D04311.

(62) Williams, J. E.; Boersma, K. F.; Le Sager, P.; Verstraeten, W. W. The high-resolution version of TM5-MP for optimized satellite retrievals: description and validation. *Geosci. Model Dev.* **2017**, *10*, 721−750.

(63) Kleipool, Q. L.; Dobber, M. R.; de Haan, J. F.; Levelt, P. F. Earth surface reflectance climatology from 3 years of OMI data. *J. Geophys. Res.-Atmos.* **2008**, *113*, D18308.

(64) Eskes, H.; Geffen, J. V.; Boersma, F.; Eichmann, K.-U.; Apituley, A.; Pedergnana, M.; Sneep, M.; Veefkind, J. P.; Loyola, D. *Sentinel-5 precursor/TROPOMI Level 2 Product User Manual Nitrogendioxide*; Ministry of Infrastructure and Water Management: 2019.

(65) Sun, K.; Zhu, L.; Cady-Pereira, K.; Chan Miller, C.; Chance, K.; Clarisse, L.; Coheur, P. F.; González Abad, G.; Huang, G.; Liu, X.; Van Damme, M.; Yang, K.; Zondlo, M. A physics-based approach to oversample multi-satellite, multispecies observations to a common grid. *Atmos. Meas. Tech.* **2018**, *11*, 6679−6701.

(66) Dunlea, E. J.; Herndon, S. C.; Nelson, D. D.; Volkamer, R. M.; San Martini, F.; Sheehy, P. M.; Zahniser, M. S.; Shorter, J. H.;

Wormhoudt, J. C.; Lamb, B. K.; Allwine, E. J.; Gaffney, J. S.; Marley, N. A.; Grutter, M.; Marquez, C.; Blanco, S.; Cardenas, B.; Retama, A.; Ramos Villegas, C. R.; Kolb, C. E.; Molina, L. T.; Molina, M. J. Evaluation of nitrogen dioxide chemiluminescence monitors in a polluted urban environment. *Atmos. Chem. Phys.* **2007**, *7*, 2691−2704.

(67) Russell, A. R.; Valin, L. C.; Bucsela, E. J.; Wenig, M. O.; Cohen, R. C. Space-based Constraints on Spatial and Temporal Patterns of NO$_x$ Emissions in California, 2005−2008. *Environ. Sci. Technol.* **2010**, *44*, 3608−3615.

(68) *Ambient Monitoring Technology Information Center (AMTIC), Environmental Protection agency, Near-road Monitoring Sites (Excel), Near-road NO2 Monitoring*. (accessed September 15).

(69) Manson, S.; Shroeder, J.; Van Riper, D.; Ruggles, S. *IPUMS National Historical Geographic Information System: Version 13.0*; Minneapolis: University of Minnesota, 2018.

(70) Hennemuth, B.; Lammert, A. Determination of the Atmospheric Boundary Layer Height from Radiosonde and Lidar Backscatter. *Boundary Layer Meteorol.* **2006**, *120*, 181−200.

(71) Dai, C.; Wang, Q.; Kalogiros, J. A.; Lenschow, D. H.; Gao, Z.; Zhou, M. Determining Boundary-Layer Height from Aircraft Measurements. *Boundary Layer Meteorol.* **2014**, *152*, 277−302.

(72) McDonald, B. C.; McKeen, S. A.; Cui, Y. Y.; Ahmadov, R.; Kim, S.-W.; Frost, G. J.; Pollack, I. B.; Peischl, J.; Ryerson, T. B.; Holloway, J. S.; Graus, M.; Warneke, C.; Gilman, J. B.; de Gouw, J. A.; Kaiser, J.; Keutsch, F. N.; Hanisco, T. F.; Wolfe, G. M.; Trainer, M. Modeling Ozone in the Eastern U.S. using a Fuel-Based Mobile Source Emissions Inventory. *Environ. Sci. Technol.* **2018**, *52*, 7360−7370.

(73) McDonald, B. C.; Dallmann, T. R.; Martin, E. W.; Harley, R. A. Long-term trends in nitrogen oxide emissions from motor vehicles at national, state, and air basin scales. *J. Geophys. Res.-Atmos.* **2012**, *117*, D00V18.

(74) Frost, G. J.; McKeen, S. A.; Trainer, M.; Ryerson, T. B.; Neuman, J. A.; Roberts, J. M.; Swanson, A.; Holloway, J. S.; Sueper, D. T.; Fortin, T.; Parrish, D. D.; Fehsenfeld, F. C.; Flocke, F.; Peckham, S. E.; Grell, G. A.; Kowal, D.; Cartwright, J.; Auerbach, N.; Habermann, T. Effects of changing power plant NO$_x$ emissions on ozone in the eastern United States: Proof of concept. *J. Geophys. Res.-Atmos.* **2006**, *111*, D12306.

(75) Jiang, Z.; McDonald, B. C.; Worden, H.; Worden, J. R.; Miyazaki, K.; Qu, Z.; Henze, D. K.; Jones, D. B. A.; Arellano, A. F.; Fischer, E. V.; Zhu, L.; Boersma, K. F. Unexpected slowdown of US pollutant emission reduction in the past decade. *Proc. Natl. Acad. Sci. U. S. A.* **2018**, *115*, 5099−5104.

(76) Judd, L. M.; Al-Saadi, J. A.; Szykman, J. J.; Valin, L. C.; Janz, S. J.; Kowalewski, M. G.; Eskes, H. J.; Veefkind, J. P.; Cede, A.; Mueller, M.; Gebetsberger, M.; Swap, R.; Pierce, R. B.; Nowlan, C. R.; Abad, G. G.; Nehrir, A.; Williams, D. Evaluating Sentinel-5P TROPOMI tropospheric NO$_2$ column densities with airborne and Pandora spectrometers near New York City and Long Island Sound. *Atmos. Meas. Tech. Discuss.* **2020**, *2020*, 1−52.

(77) Griffin, D.; Zhao, X.; McLinden, C. A.; Boersma, F.; Bourassa, A.; Dammers, E.; Degenstein, D.; Eskes, H.; Fehr, L.; Fioletov, V.; Hayden, K.; Kharol, S. K.; Li, S.-M.; Makar, P.; Martin, R. V.; Mihele, C.; Mittermeier, R. L.; Krotkov, N.; Sneep, M.; Lamsal, L. N.; Linden, M. t.; van Geffen, J.; Veefkind, P.; Wolde, M. High-Resolution Mapping of Nitrogen Dioxide With TROPOMI: First Results and Validation Over the Canadian Oil Sands. *Geophys. Res. Lett.* **2019**, *46*, 1049−1060.

(78) Pope, R. J.; Graham, A. M.; Chipperfield, M. P.; Veefkind, J. P. High resolution satellite observations give new view of UK air quality. *Weather* **2019**, *74*, 316−320.

(79) Goldberg, D. L.; Lu, Z.; Streets, D. G.; de Foy, B.; Griffin, D.; McLinden, C. A.; Lamsal, L. N.; Krotkov, N. A.; Eskes, H. Enhanced Capabilities of TROPOMI NO$_2$: Estimating NO$_x$ from North American Cities and Power Plants. *Environ. Sci. Technol.* **2019**, 12594.

(80) Ialongo, I.; Virta, H.; Eskes, H.; Hovila, J.; Douros, J. Comparison of TROPOMI/Sentinel 5 Precursor NO$_2$ observations with ground-based measurements in Helsinki. *Atmos. Meas. Tech.* **2020**, *13*, 205−218.

(81) McLinden, C. A.; Fioletov, V.; Boersma, K. F.; Kharol, S. K.; Krotkov, N.; Lamsal, L.; Makar, P. A.; Martin, R. V.; Veefkind, J. P.; Yang, K. Improved satellite retrievals of NO_2 and SO_2 over the Canadian oil sands and comparisons with surface measurements. *Atmos. Chem. Phys.* **2014**, *14*, 3637−3656.

(82) Zhang, Y.; Wang, Y.; Chen, G.; Smeltzer, C.; Crawford, J.; Olson, J.; Szykman, J.; Weinheimer, A. J.; Knapp, D. J.; Montzka, D. D.; Wisthaler, A.; Mikoviny, T.; Fried, A.; Diskin, G. Large vertical gradient of reactive nitrogen oxides in the boundary layer: Modeling analysis of DISCOVER-AQ 2011 observations. *J. Geophys. Res.: Atmos.* **2016**, *121*, 1922−1934.

(83) Houston, D.; Li, W.; Wu, J. Disparities in Exposure to Automobile and Truck Traffic and Vehicle Emissions Near the Los Angeles−Long Beach Port Complex. *Am. J. Public Health* **2014**, *104*, 156−164.

(84) Houston, D.; Wu, J.; Ong, P.; Winer, A. Structural disparities of urban traffic in Southern California: Implications for vehicle-related air pollution exposure in minority and high-poverty neighborhoods. *J. Urban Affairs* **2004**, *26*, 565−592.

(85) Houston, D.; Krudysz, M.; Winer, A. Diesel Truck Traffic in Low-Income and Minority Communities Adjacent to Ports:Environmental Justice Implications of Near-Roadway Land Use Conflicts. *Transp. Res. Rec.* **2008**, *2067*, 38−46.

(86) Lena, T. S.; Ochieng, V.; Carter, M.; Holguín-Veras, J.; Kinney, P. L. Elemental carbon and $PM_{2.5}$ levels in an urban community heavily impacted by truck traffic. *Environ. Environ. Health Perspect.* **2002**, *110*, 1009−1015.

(87) Karner, A.; Eisinger, D.; Bai, S.; Niemeier, D. Mitigating Diesel Truck Impacts in Environmental Justice Communities:Transportation Planning and Air Quality in Barrio Logan, San Diego, *California*. *Transp. Res. Rec.* **2009**, *2125*, 1−8.

(88) Marr, L. C.; Harley, R. A. Modeling the Effect of Weekday-Weekend Differences in Motor Vehicle Emissions on Photochemical Air Pollution in Central California. *Environ. Sci. Technol.* **2002**, *36*, 4099−4106.

(89) Nassar, R.; Napier-Linton, L.; Gurney, K. R.; Andres, R. J.; Oda, T.; Vogel, F. R.; Deng, F. Improving the temporal and spatial distribution of CO_2 emissions from global fossil fuel emission data sets. *J. Geophys. Res.: Atmos.* **2013**, *118*, 917−933.

(90) McDonald, B. C.; McBride, Z. C.; Martin, E. W.; Harley, R. A. High-resolution mapping of motor vehicle carbon dioxide emissions. *J. Geophys. Res.: Atmos.* **2014**, *119*, 5283−5298.

(91) Zoogman, P.; Liu, X.; Suleiman, R. M.; Pennington, W. F.; Flittner, D. E.; Al-Saadi, J. A.; Hilton, B. B.; Nicks, D. K.; Newchurch, M. J.; Carr, J. L.; Janz, S. J.; Andraschko, M. R.; Arola, A.; Baker, B. D.; Canova, B. P.; Chan Miller, C.; Cohen, R. C.; Davis, J. E.; Dussault, M. E.; Edwards, D. P.; Fishman, J.; Ghulam, A.; González Abad, G.; Grutter, M.; Herman, J. R.; Houck, J.; Jacob, D. J.; Joiner, J.; Kerridge, B. J.; Kim, J.; Krotkov, N. A.; Lamsal, L.; Li, C.; Lindfors, A.; Martin, R. V.; McElroy, C. T.; McLinden, C.; Natraj, V.; Neil, D. O.; Nowlan, C. R.; OSullivan, E. J.; Palmer, P. I.; Pierce, R. B.; Pippin, M. R.; Saiz-Lopez, A.; Spurr, R. J. D.; Szykman, J. J.; Torres, O.; Veefkind, J. P.; Veihelmann, B.; Wang, H.; Wang, J.; Chance, K. Tropospheric emissions: Monitoring of pollution (TEMPO). *J. Quant. Spectroscopy Rad. Transfer* **2017**, *186*, 17−39.